Catalysis Today xxx (xxxx) xxx

Contents lists available at ScienceDirect

Catalysis Today

journal homepage: www.elsevier.com/locate/cattod

How does the balance of metal and acid functions on the benchmark Mo/ZSM-5 catalyst drive the Methane dehydroaromatization reaction?

Antoine Beuque [a,*], Hao Hu [b], Elise Berrier [b], Alexander Sachse [a], Jean-François Paul [b], Ludovic Pinard [a,*]

[a] Institut de Chimie des Milieux et Matériaux de Poitiers (ICM2P), UMR 7285 CNRS, 4 Rue Michel Brunet, Bâtiment B27, 86073 Cedex 9 Poitiers, France
[b] Univ. Lille, CNRS, Centrale Lille, Univ. Artois, UMR 8181–UCCS–Unité de Catalyse et Chimie du Solide, F-59000 Lille, France

ARTICLE INFO

Keywords:
Zeolite
Methane dehydroaromatization
Molybdenum species
Brønsted acidity
Catalytic activity
Deactivation

ABSTRACT

Among all the proposed catalytic systems (new supports, synthesis post-treatment, change of transition metal, multi-metallic catalysts, etc.) for the methane dehydroaromatization, the initial Mo/ZSM-5 has remained one of the best suitable catalysts, despite its lack of deep understanding. The catalyst evolves throughout four successive stages: calcination, activation, induction, and deactivation. By studying the balance influence between the acid and metal functions throughout its lifetime, the molybdenum and carbon species could be localized, quantified, and identified as well as their roles. An optimal compromise was then established where the catalyst is composed of 4 wt% Mo with the highest possible acidity. Below these targets, the catalysts with minimal Mo content and low Brønsted acidity display poor catalytic performances, whereas zeolite amorphization occurs during the early stages of the reaction independently of the zeolite acidity once the Mo loading exceeds the optimal value.

1. Introduction

The depletion of the worldwide crude oil reserves and its price instability have shifted the appeal of new energy sources towards natural gas. The 40% increase in natural gas production in the past decade [1,2] has raised significant interest in developing innovative use for natural gas as a new chemical reactant. Methane, the most abundant compound in natural gas, is primarily used for electricity supply. As only 1.5% of natural gas is catalytically converted into building block molecules, groundbreaking methods for the transformation of methane are considerably required [3,4].

Non-oxidative Methane Dehydroaromatization (MDA: 6 $CH_4 \leftrightharpoons C_6H_6 + 9\ H_2$) on bifunctional catalyst Mo/ZSM-5 has arisen as a key technology to decarbonize natural gas to high-value chemicals and CO_2 free clean energy vectors. However, MDA faces two major hurdles: (i) low activity, as the one-pass conversion into benzene is thermodynamically limited (~12% at 700 °C) and (ii) rapid catalyst deactivation, as coke formation is kinetically favored at high temperature [5–7].

Ever since the singular bifunctional Mo/ZSM-5 active MDA catalyst reported by Wang et al. in 1993 [8], considerable interest has been paid over the past three decades to unravel the secrets of MDA. Briefly, the MDA process occurs through four successive steps: (i) catalyst preparation generally consisted of an incipient wetness impregnation followed by a calcination [9], (ii) activation where no aromatic production is observed corresponding to the reduction of the molybdenum oxide into molybdenum carbide centres [10,11] (iii) the latter converts methane to olefin intermediates initiating aromatic formation during the induction step [12,13] (iv) once the catalyst achieves is operational activity, it begins to deactivate [14,15].

Numerous transition metals were tested (Cr, V, Fe, W,…), and molybdenum was considered the best suitable one [16]. However, molybdenum alone is insufficient to produce benzene, even though Mo impregnated silicalite shows low MDA activity [17]. The Brønsted acid sites (BAS) and the shape selectivity provided by the ZSM-5 zeolite are necessary to assist in the formation of benzene [18].

The role of the Brønsted acid sites (BAS) was evidenced: (i) Low Si/Al molar ratio allows highly dispersing the Mo precursor for active sites inside the zeolite channels during the calcination step due to cation exchange with protons [19]. (ii) High BAS density favors the aromatization of coke precursors leading to carbon accumulation, hence catalyst deactivation [20,21]. The acidity plays, therefore, a unique dual role in which it allows the molybdenum dispersion inside the zeolite channel while favoring the catalyst deactivation. Carefully tuning the catalyst acidity has been revealed to be one of the main research topics in MDA

* Corresponding authors.
E-mail addresses: antoine.beuque@univ-poitiers.fr (A. Beuque), ludovic.pinard@univ-poitiers.fr (L. Pinard).

https://doi.org/10.1016/j.cattod.2022.06.001
Received 31 December 2021; Received in revised form 17 May 2022; Accepted 1 June 2022
Available online 6 June 2022

and widely discussed in the literature.

Considerable effort has been devoted to modifying the catalyst acidity before and after impregnation: modification of the Si/Al molar ratio [22,23], partial alkali-cation exchange [24,25], neutralization of the external BAS by silylation [26], use of a bimetallic catalyst with the addition of a dopant (Cr, Ag, …) [27]. However, all these modifications show no significant stability benefit. Indeed, after a short period of catalyst stability enhancement, it finally deactivates.

All these previous investigations questioned the catalyst acidity involvement in the reaction and put back in the heart of the discussion the molybdenum influence. Indeed, among all the proposed catalytic systems, the initial Mo/ZSM-5 catalyst has remained one of the most promising catalysts for this reaction, hence arousing the curiosity of the whole scientific community. For years, the ideal catalyst balance was proposed to be ~5 wt% of molybdenum with Si/Al ratios in the range of 15–40 [7]. However, more recently, several groups reported a significant stability [23,28,29] and benzene selectivity [30] enhancement as the Mo loading increases until 16 wt%. Thus, this lack of information and general agreement encouraged our following study.

Here, we address the tuning of the balance between the two catalyst functions involved in the MDA, namely the metallic and acid functions. The influence of the Mo loading (up to 20 wt%) on the zeolite with various BAS concentrations (SiAl = 15, 25, 40, 75, and ∞) was systematically investigated throughout the four successive reaction stages. It provides new insights and adjusts some interpretations of the literature. For each unique Si/Al molar ratio, particular attention was paid to the location, nature, quantification, and evolution of the molybdenum species, which allow us to separate the active from the spectator species and elucidate their clear role in the reaction. In particular, it was proposed how solely the molybdenum drives the reaction independent of the zeolite acidity once its amount exceeds a general value of 4 wt%.

2. Experimental

2.1. Catalyst preparation

As starting materials, NH_4-ZSM-5 zeolites CBV 3024E, CBV 5020, CBV 8014, and CBV 1502 provided by Zeolyst International with a molar Si/Al ratio = 15, 25, 40, and 75 respectively were converted into protonic ZSM-5 zeolites by calcining the initial materials under static air conditions at 550 °C for 6 h with a heating rate of 2 °C min^{-1}. The protonic zeolite was denoted HZ-Y, where Y refers to the Si/Al molar ratio. HZSM-5 supported Mo catalysts were prepared by traditional incipient wetness impregnation aqueous solution of ammonium heptamolybdate tetrahydrate (AHM, $(NH_4)_6Mo_7O_{24}.4H_2O$, Sigma Aldrich) with a wide concentration range from 0.0015 M to 0.030 M. The Mo loading target was calculated from 1 wt% to 20 wt%. 50 mL of the following solution of protonic zeolite was added dropwise per gram of protonic zeolite under magnetic stirring (400 rpm) at room temperature for 24 h. Then, the catalyst was dried under static air at 80 °C for 12 h and calcined at 500 °C using a heating ramp of 2 °C min^{-1} for 6 h. The resulting Mo-supported catalysts were denoted X-MoHZ-Y, where X represents the Mo loading directly calculated by ICP measurement and Y the molar Si/Al given by the supplier (Zeolyst International).

Additionally, a silicalite was synthesized according to the procedure detailed in the following section [31]. Then, molybdenum impregnation was carried out with the same protocol described previously. As a result, the samples are denoted X-Si.

2.2. Catalyst characterization before the catalytic test

Powder X-ray diffractograms were collected with a PANalytical Empyrean X-ray diffractometer with Cu Kα radiation (λ = 0.15418 nm), for the 2θ range from 5° to 50°. The scan speed was fixed at 0.033° s^{-1}. The size of the MoO_3 crystallites was calculated employing the well-known Scherrer equation:

$$B(2\theta) = \frac{K\lambda}{Lcos(\theta)} \quad (1)$$

whereB is the full width at maximum, also known as FWHM K is the crystal shape factor given as 0.9.

λ is the wavelength of X-rays (0.15406 nm for the Cu).

L is the crystal size (nm).

θ is the Bragg's angle (radian).

The molybdenum content of X-MoHZ-Y was directly determined using Inductively Coupled Plasma-Optical Emission Spectroscopy (ICP-OES) on an Optima 2000 DV (Perkin-Elmer). Before the measurement, all samples were dissolved in an acid mixture composed of 4 mL HNO_3 (68%), 2 mL HCl (34–37%), 2 mL HF (47–51%), and 42 mL H_2O and mineralized in Anton-Paar Multiwave pro microwave.

The morphology, homogeneity, and particle size were determined using a Scanning Electron Microscope (SEM) (Philips XL30 FEG).

Nitrogen sorption measurements were carried out at −196 °C on the zeolite before and after wetness impregnation with a Micromeritics 3Flex apparatus. Samples were outgassed at room temperature under vacuum for 15 h before the sorption measurements. The micropore volume (V_{micro}) was calculated from the t-plot curve using the Harkins-Jura method and a thickness range between 4.5 and 5.5 Å. The mesopore volume (V_{meso}) was deduced by subtracting the total pore volume taken at $P/P_0 = 0.95$ and the micropore volume.

The nature and concentration of acidity of the zeolite before and after Mo impregnation were studied using pyridine adsorption followed by infrared spectroscopy (FTIR) with a Nicolet 5700 apparatus with 2 cm^{-1} optical resolution. Before analysis, samples were pressed (0.5 ton) into a self-supporting wafer (2 cm^2), then pre-treated from 20 °C to 450 °C under 100 mL min^{-1} of air stream with a rate of 2 °C min^{-1}. The sample was then degassed for 1 h at 200 °C, after which an IR spectrum was taken. The sample was then cooled down to 150 °C, exposed to a pyridine pressure of 1.5 10^{-3} bar for 5 min, and then further degassed for 1 h before recording the spectra. The concentration of Brønsted (PyH^+) and Lewis acid sites (PyL) (μmol g^{-1}), were calculated using the Beer-Lambert-Bouguer law from the integrated absorbance of the corresponding IR bands (1545 and 1455 cm^{-1}) and the integrated molar adsorption coefficients: $\varepsilon_{1545} = 1.13$ and $\varepsilon_{1454} = 1.28$ cm mol^{-1}. [32].

Raman spectra of fresh catalysts were recorded using the 488 line of a Ar^+-ion laser (Melles Griot) focused on the sample using a 100X microscope objective (NA=0.9, Olympus). The scattered light was guided through a 150 μm confocal hole analysed by means of a 1800 grooves grating and Peltier-cooled CCD (ANDOR) as implemented in the Labram HR spectrometer (HORIBA).

2.3. Catalytic evaluation

Methane dehydroaromatization was performed at atmospheric pressure in a fixed-bed quartz reactor (6 mm inner diameter) at 700 °C under continuous feeding of a (15/85) (v/v) N_2/CH_4 mixture (Air Liquid, purity: 99.999) using a constant flow rate of 0.84 L h^{-1} (STP). The methane gas hourly space velocity per gram of catalyst (M-GHSV) was 1.4 L h^{-1} g_{cat}^{-1} which is commonly used for this reaction [16]. Before testing, catalysts were compacted under 3 tons, crushed, and sieved to obtain homogeneous particles (0.2–0.4 mm), then 0.6 g of the sieved catalyst was loaded inside the reactor. Firstly, all samples were pre-treated at 700 °C under nitrogen flow (3 L h^{-1}) for 1 h, using a heating ramp of 10 °C min^{-1}.

The gaseous products and hydrogen were analyzed online by a Varian CP-3800 gas chromatograph equipped with an FID detector connected to a fused silica J&W GS-Gaspro capillary column (60 m x 0.32 mm × 4 μm), and a TCD connected to a J&W PoraPLOT Q-HT capillary column (25 m x 0.53 mm × 20 μm). The GC analysis time was 30 min and therefore does not allow data to be obtained during the activation and induction periods occurring during the first tens of reaction minutes. For that reason, an HPR 20 QIC R&D mass spectrometer

(Hiden Analytical) was also connected to the exhaust gas to monitor as a function of time-on-stream the mass-to-charge ratio 16, 27, 78, 92, and 128, which corresponds to CH_4, $C_2H_3^+$, C_6H_6, C_7H_8, and $C_{10}H_8$, respectively.

2.4. Spent catalyst characterization after the catalytic test

After 10 h, the feed gas was stopped, and the reactor was rapidly cooled down to 150 C using an external airflow. The recovered materials were named X-MoHZ-Y/Sp. Coke amount was quantified with a SDT Q600 under a flow rate of 100 mL min^{-1} of air up to 900 °C. After loading the TG cell, the sample was firstly kept for 30 min in a dry air stream. The sample was then heated with a rate of 20 °C min^{-1}. Once the final temperature reached, the plateau was held for 10 min. Burning gas, i.e., H_2O ($m/z = 18$), CO ($m/z = 28$), and CO_2 ($m/z = 44$) were monitored by mass spectra (QGA.

Hiden Analytical). Residual microporosity, XRD pattern, and Mo content were measured using the same protocol as previously described.

3. Results

3.1. Structure and density of the molybdenum species on the supported oxomolybdate zeolite X-HZ-Y after calcination

Table 1 gathers all the characterization data calculated for each sample. The samples are denoted X-MoHZ-Y, where X refers to the amount of molybdenum deposited on the fresh catalyst directly established from ICP measurement. As for Y, it represents the molar Si/Al molar ratio given by the zeolite supplier, i.e., Zeolyst international.

Firstly the morphology, crystallinity of the samples were investigated. Then, particular attention was paid to the identification and localization of the oxo-molybdate species to properly quantify their impact on the textural properties of the protonic zeolites.

Powder X-ray diffraction analyses (XRD) of the supported oxomolybdate zeolites X-HZ-Y are presented in **Figure S.1**. The peaks ascribed to the MFI framework at 7.9°, 8.8°, 23.0°, 23.9°, and 24.3° keep their initial intensity irrespective of the Mo loading. No MFI peak shifts were observed with respect to the Mo loading. On the other hand, the characteristic peaks of the orthorhombic MoO_3 crystallites at 12.7°,

Table 1
Characterization data of the supported oxo-molybdate fresh catalysts after the calcination step normalized from the zeolite and catalyst amount.

Sample name	Mo (wt%)[a]	Micropore volume[b]		Mesopore volume[c]		$[H^+]$ neutralized[d]		MoO_3 crystallite size[e]
		$cm^3.\ g_{cat}^{-1}$	$cm^3.\ g_z^{-1}$	$cm^3.\ g_{cat}^{-1}$	$cm^3.\ g_z^{-1}$	µmol. g_{cat}^{-1} (i)	µmol. g_z^{-1} (ii)	nm
Series 15								
HZ-15	0	0.13	0.13	0.06	0.06	0	0	0
0.7-MoHZ-15	0.7	0.13	0.13	0.06	0.06	74	71	0
1.6-MoHZ-15	1.6	0.12	0.13	0.06	0.06	122	116	0
4.0-MoHZ-15	4.0	0.12	0.13	0.05	0.05	156	141	66
4.9-MoHZ-15	4.9	0.12	0.12	0.05	0.05	184	167	73
7.4-MoHZ-15	7.4	0.10	0.11	0.04	0.04	115	84	106
11.4-MoHZ-15	11.4	0.10	0.12	0.04	0.05	158	113	93
16.1-MoHZ-15	16.1	0.08	0.11	0.04	0.05	209	152	97
Series 25								
HZ-25	0	0.14	0.14	0.09	0.09	0	0	0
1.0-MoHZ-25	1.0	0.14	0.14	0.06	0.06	76	74	0
2.0-MoHZ-25	2.0	0.13	0.13	0.07	0.07	107	103	0
3.5-MoHZ-25	3.5	0.13	0.14	0.06	0.06	70	62	78
4.1-MoHZ-25	4.1	0.13	0.14	0.06	0.06	85	76	81
9.8-MoHZ-25	9.8	0.13	0.14	0.04	0.04	/	/	93
13.6-MoHZ-25	13.6	0.12	0.14	0.04	0.05	86	53	97
18.8-MoHZ-25	18.8	0.11	0.13	0.04	0.05	/	/	97
Series 40								
HZ-40	0	0.16	0.16	0.05	0.05	0	0	0
0.8-MoHZ-40	0.8	0.15	0.15	0.07	0.07	13	11	0
2.1-MoHZ-40	2.1	0.15	0.15	0.07	0.07	6	1	80
4.0-MoHZ-40	4.0	0.15	0.15	0.05	0.05	7	-3	82
5.2-MoHZ-40	5.2	0.15	0.15	0.04	0.04	/	/	93
7.3-MoHZ-40	7.3	0.14	0.15	0.04	0.04	24	6	91
13.1-MoHZ-40	13.1	0.12	0.14	0.05	0.06	36	3	98
18.8-MoHZ-40	18.8	0.11	0.14	0.03	0.04	42	-6	97
Series 75								
HZ-75	0	0.15	0.15	0.05	0.05	0	0	0
0.8-MoHZ-75	0.8	0.15	0.15	0.05	0.05	0	-1	0
2.6-MoHZ-75	2.6	0.14	0.14	0.05	0.05	-8	-12	80
4.0-MoHZ-75	4.0	0.14	0.15	0.05	0.05	6	0	89
7.3-MoHZ-75	7.3	0.13	0.14	0.03	0.03	11	1	105
8.9-MoHZ-75	8.9	0.13	0.15	0.03	0.03	12	0	101
13.2-MoHZ-75	13.2	0.13	0.14	0.03	0.04	24	7	98
16.9-MoHZ-75	16.9	0.12	0.14	0.03	0.04	28	6	99
Silicalite								
Si		0.18	0.18	0	0	0	0	0
1.6-Si	1.6	0.16	0.16	0	0	0	0	0
2.6-Si	2.6	0.17	0.17	0	0	0	0	0
6.3-Si	6.3	0.15	0.16	0	0	0	0	95

[a] Mo content measured by ICP analysis, b micropore volume estimated with t-plot,
[b] The micropore volume (Vmicro) was calculated from the t-plot curve using the Harkins-Jura method and a thickness range between 4.5 and 5.5 Å,
[c] The mesopore volume was deduced with the subtraction of the total pore volume taken at P/P0 = 0.95 minus the micropore volume,
[d] The neutralized Brønsted probed by thermodesorption of pyridine at 150 °C (i) was normalized from the amount of catalyst, i.e., Eq.S1 and (ii) normalized from the amount of zeolite, i.e., Eq.S2.
[e] The MoO3 crystallite size was deduced from the Scherrer equation. The data were normalized either to the total amount of catalyst (gcat) or the zeolite amount.

25.7°, and 27.3 [33] (JCPDS File No. 04–012–8070) start to appear for Mo content higher than 3–4 wt%.

Contrary to other suggestions [34,35], no other phase, e.g., $Al_2(MoO_4)_3$, was detected on the XRD patterns. No extraction of framework Al from the zeolite, even with a high Mo content, i.e.,> 8 wt %, occurs during the calcination.

From the XRD patterns (Fig. S1), it is possible to calculate the size of the MoO_3 particle with the Scherrer equation (Eq. 1). The resulting measure is plotted as a function of Mo loading (Fig. 1). It appears that the crystal MoO_3 size is independent of the Si/Al ratio. Additional SEM analyses show the morphology of the MoO_3 particles deposited at the external surface for various Mo loading.

Three different areas can be identified and classified with ascending Mo content: (i) Mo < 5 wt%: the MoO_3 crystallite size range is between 60 nm and 90 nm. Very isolated particles were detected, (ii) 5 wt% ≤ Mo ≤ 13 wt% the particles MoO_3 size remains constant at ~ 90 nm, and SEM images support higher MoO_3 density on the external surface and (iii) Mo > 13 wt%: the MoO_3 particles are highly dispersed within the zeolite micro-crystal, forming a well uniform solid mixture where the remaining MoO_3 "dilute" the zeolite catalyst to a certain extent.

The size of the MoO_3 particle (~ 90 nm) is too large for diffusing inside the internal HZSM-5 zeolite channels (5.5 * 5.1 Å and 5.3 * 5.6 Å) [36].

N_2-physisorption measurements were carried out to probe more deeply the internal structure of the catalyst. From Table 1, microporous volumes between 0.13 – 0.16 $cm^3\ g_z^{-1}$ were deduced for the protonic zeolites.

Once the molybdenum is impregnated on the commercial zeolite, it is crucial to make two distinctions:

(i) Normalization from the amount of the total catalyst (g_{cat})
(ii) Normalization from the amount of only the zeolite by removing the molybdenum content directly calculated from the ICP measurement (g_z)

Indeed, as explained previously and observed on SEM analysis, a high amount of molybdenum "dilutes" the zeolite crystal. Therefore, this differentiation allows probing more precisely the textural properties of the zeolite by removing the impact of this "diluting effect" on the zeolite crystal and avoiding any misleading interpretation.

V_{micro} for each catalyst was calculated using the two different normalization modes and summarized in Table 1. Fig. 2 shows the calculated V_{micro} plotted as a function of the Mo loading for each series.

By considering V_{micro}^{cat} (Fig. 2**.a.**) normalized with the full catalyst mass, it would appear that increasing the impregnated molybdenum content strongly decreases the micropore volume. Thus, leading to a probable crystallinity loss. Pinglian [28] also made a similar comment and ranked the microporous volume by descending order: HZSM-5 > 6 wt% Mo/HZSM-5 > 10 wt% Mo/HZSM-5.

On the other hand, another trend emerges by removing the excess of MoO_3 in the calculation of the micropore volume (V_{micro}^{z}) (Fig. 2**. b**). Indeed, the zeolite micropore volume seems to stay constant regardless of the Mo content. Thus a negligible loss of crystallinity occurs when the Mo loading increases. However, despite the low calcination temperature, V_{micro}^{z} still slightly decreases with high Mo loading for the series SiAl = 15, which is due to the possible formation of extra-framework species such as $Al_2(MoO_4)_3$.occurring favorably for low Si/Al molar ratio. ^{27}Al MAS NMR confirmed the presence of such species (Fig. S2).

The nitrogen adsorption analyses are an excellent example of the previous distinction made, i.e., the normalization calculation, originating from the "diluting effect" of the MoO_3 particles.

Ex-situ Raman spectroscopy was used as a powerful tool for investigating the structure of the supported phase. Due to the numerous molybdenum configurations on zeolite, the assignment of Raman lines of both bulk and supported Mo oxides has been widely discussed in literature [37–39]. The *ex-situ* Raman spectra of the fresh catalysts are shown in Fig. 3.

Catalysts with Si/Al molar ratios of 15, 25, and 40 (Fig. 3**. a-b-c**) follow a similar trend. Three different sections have been identified.

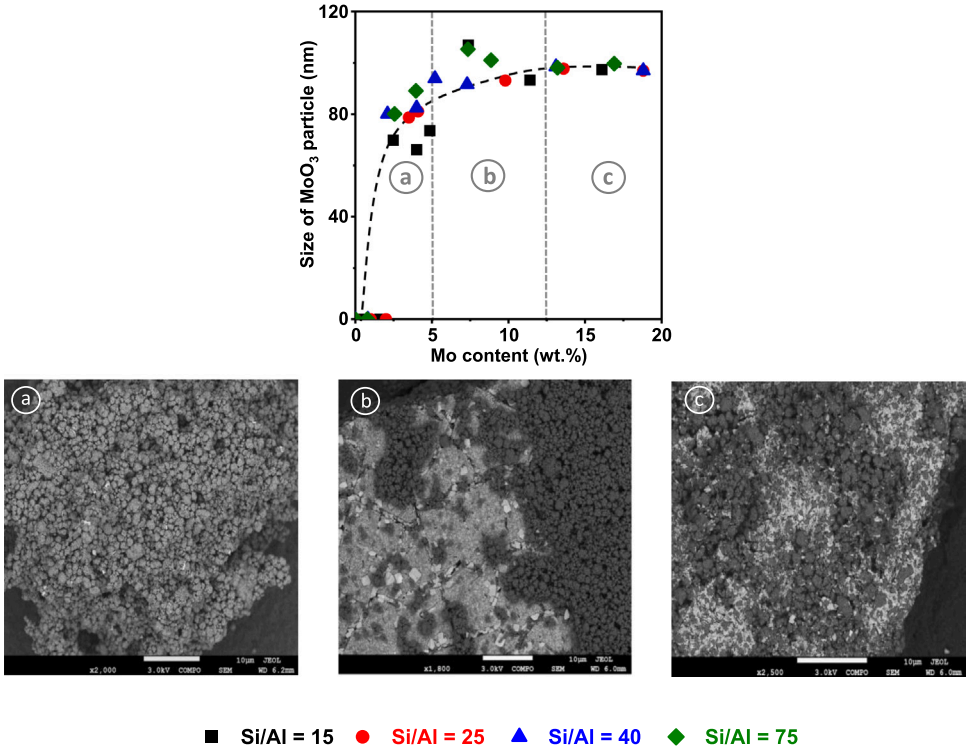

Fig. 1. : Size of the MoO_3 crystallites deposited at the external zeolite surface calculated with the Scherrer equation as a function of the Mo loading. The associated TEM micrographs of molybdenum crystallites are given for different molybdenum amounts.

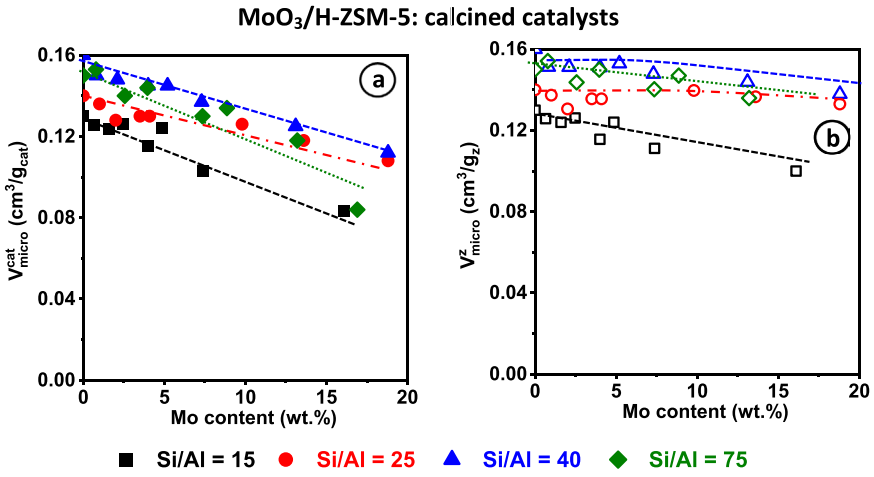

Fig. 2. Microporous volume per catalyst weight V_{micro}^{cat} (a) and per zeolite weight V_{micro}^{z} (b) as a function of the Mo loading for the different catalyst series.

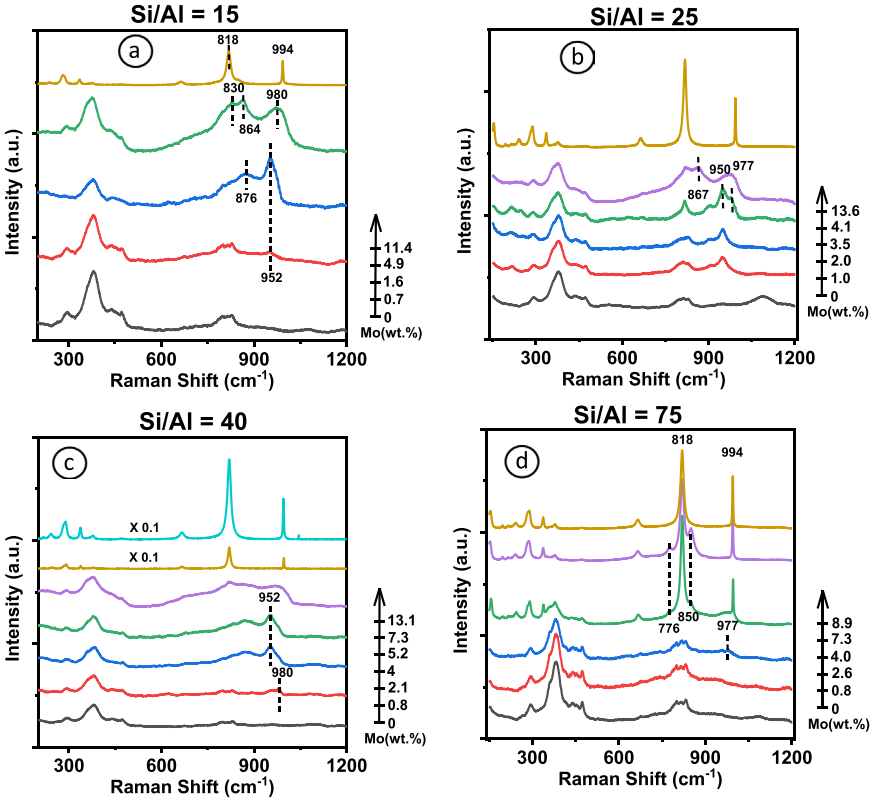

Fig. 3. Raman spectra of the calcined catalysts as a function of the Mo loading for the different catalyst series: (a) SiAl = 15; (b) SiAl = 25; (c) SiAl = 40 and (d) SiAl = 75.

- At 1% Mo loading, our results suggest the presence of either hydrated isolated moieties or [$AlMo_6$] species. Indeed, the spectrum present ν(Mo═O) stretch vibration at 960–975 cm^{-1} indicating hydrated monomeric supported MoO_x species. In addition, the characteristic lines of bulk Anderson-type [$AlMo_6$] hetero-polymolybdate $(NH_4)_3[Al(OH)_6Mo_6O_{18}]$ at 900 and 944 cm^{-1} were also noted.

- When the Mo content increases until ~ 4 wt%, a supported poly-oxomolybdate phase develops, as supported by the increase of the broad scattering centered around 850 cm^{-1}. In general, the relative intensity of the 850–880 cm^{-1} signal compared to the 950–975 cm^{-1} one is a fair indicator of the polymerization degree. The polymeric entities Mo_xO_y are also observed at higher Raman frequency (960–985 cm^{-1}), indicating ν(Mo═O) stretch vibration.
- When the Mo loading exceeds 4 wt% Mo, intense and sharp Raman lines at 818 and 994 cm^{-1} start to emerge, meaning the α-MoO_3 phase is detected. Its relative intensity increases with increasing Mo content until becoming the only detected phase owing to the large Raman cross-section of α-MoO_3 as compared to the other oxomolybdate moieties.

The catalyst with a Si/Al molar ratio of 75 (Fig. 3**d**) shows a specific evolution upon Mo loading. At 3% Mo loading, lines at 975, 955, 818, and 615 cm^{-1} were detected, implying Mo stands as silico-molybdic acid $H_4SiMo_{12}O_{40}$. Increasing the Mo content, the β-MoO_3 phase

metastable were identified as shown by the typical lines at 904 (medium), 849 (very strong), and 774 (strong) cm^{-1}. The β-MoO_3 phase develops parallel to α-MoO_3, but no polymeric oxomolybdate phase has been evidenced. At 10% Mo content, the only detected phase is α-MoO_3.

Raman spectroscopy evidences the dimerization of two molybdenum monomers MoO_x to form poly-oxomolybdate at a low Si/Al ratio once the Mo content reaches a specific value. No poly-oxomolybdate was identified for a higher Si/Al molar ratio.

IR analyses were carried out to gain insight into the localization of the different Molybdenum moieties. Fig. 4 compares the infrared spectra in the OH stretching region as a function of molybdenum content on the four catalysts series.

The infrared spectra in the OH stretching region of the protonic zeolite (dashed lines) exhibit five well-known bands. An intense band at 3610 cm^{-1} (± 2) assigned to the bridged hydroxyl groups (Si-O(H)-Al); an asymmetric band at 3740 cm^{-1} ascribable to the terminal silanol groups on the external surface, two bands at 3665 cm^{-1}, and 3785 cm^{-1} (less intense), which correspond to OH linked to extra-framework aluminum species (e.g., $AlOH^+$) and finally a broad shoulder centered at 3470 cm^{-1} attributed to Si-OH of the hydroxyl nests considered as internal defects.

Once the molybdenum is impregnated, one common observation emerges: the external silanol stretching band intensity decreases as the molybdenum content increases. By analogy with Al pairs, the assumption was established that vicinal silanol could also react with molybdenum oxide. However, it is impossible to discriminate between monomeric or dimeric molybdenum anchored silanol species with the IR OH spectra.

Separating the series is necessary for the following considerations.

- SiAl = 15 (Fig. 4**a**), the intensity of the bridged hydroxyl groups decreases and reaches a plateau when the Mo content is 1.6 wt%. The same observation occurs for the EFAL intensity band. Once the Mo content achieves 11.4 wt%, the intensity of the EFAL band increases probably due to the formation of $Al_2(MoO_4)_3$, which is supported by the loss of micropore volume. The molybdenum extracts the aluminum framework and creates EFAL species.
- SiAl = 25 (Fig. 4**b**), the band intensity at 3610 cm^{-1} starts to decrease at low Mo content (< 2 wt%). Once this value is reached, its intensity stays constant. As for the EFAL band intensity, it reduces as the Mo amount increases until it totally disappears at high Mo content. Contrary to the series SiAl = 15, it suggests the molybdenum reacts with EFAL and preserves the internal zeolite crystallinity.
- SiAl = 40 (Fig. 4**c**), the intensity of the bridged OH-band remains constant irrespective of the Mo content supporting; thus, molybdenum is not anchored on Brønsted acid sites. More surprisingly, the shoulder band at 3470 cm^{-1} indicating the silanol nests reacts with the molybdenum. One possible synthesized species is single site Mo-containing ZSM-5 as reported by Mintova et coll [40,41], who illustrated the isomorphous substitution framework Si atoms with

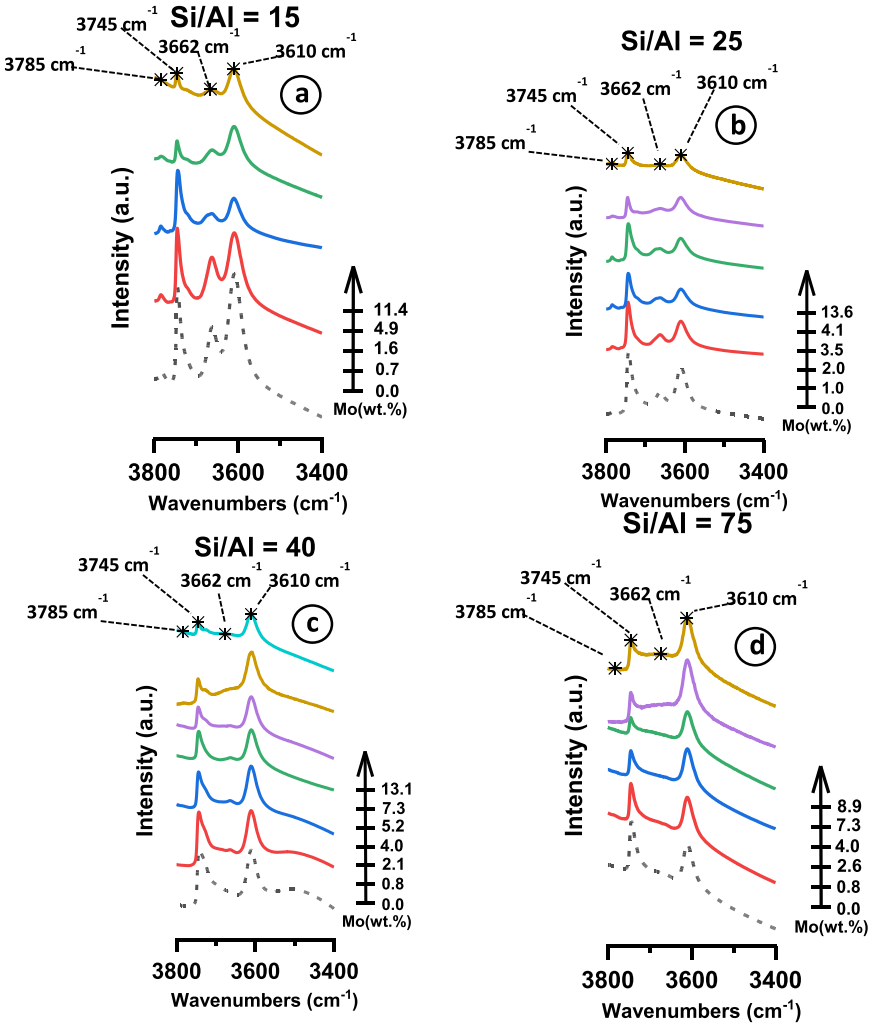

Fig. 4. : IR spectra of OH region of the calcined catalysts as a function of the Mo loading for the different catalyst series: (a) SiAl = 15; (b) SiAl = 25; (c) SiAl = 40 and (d) SiAl = 75. The spectra intensity was normalized from the zeolite amount.

Mo atoms in Silicalite-1 zeolite under specific conditions. However, the XRD patterns presented in Fig. S1 are not appropriate for the detection of this species. Indeed, the Mo framework zeolite is monoclinic, leading to peak splitting of the XRD pattern between 2Θ= 22–26.5°. Such characteristics are not observed. Therefore, the formation of these species still needs to be further elucidated.

- SiAl = 75 (Fig. 4**d**), aside from the silanol band previously explained all other stretching OH bands display equal intensity confirming that no molybdenum is anchored on Brønsted acid sites inside the zeolite channel.

From the chemisorption of pyridine at 150 °C, it is possible to quantify the number of anchored oxo-molybdate species inside the zeolite channel. The calculated Brønsted acidity on the four protonic zeolites are (ascending order of Si/Al molar ratio): 504, 290, 250, and 138 μmol g_z^{-1}.

Fig. 5 displays the neutralized Brønsted acid sites as a function of the Mo loading for each different series. As for the N_2-physisorption measurement, a mass correction coefficient is also necessary to correctly quantify the pyridine chemisorption at 150 °C of the supported oxo-molybdate phase.

First of all, it appears that after Mo impregnation, the BAS concentration decreases compared with the parent zeolite indicating molybdenum oxide reacts with available proton during the calcination step. In addition, the lower the Si/Al (high BAS concentration), the higher the quantity of neutralized BAS.

However, a non-negligible difference occurs between the two normalization modes. In Fig. 5**a**, it seems that the neutralized BAS keeps increasing as a function of Mo impregnated amounts. More surprising, for the series SiAl = 40 and 75, the neutralized BAS is directly related to the Mo content. This proportionality link indicates the need to use the second normalization method, i.e., per gram of zeolite. By taking into account, this correction (Fig. 5**b**), the neutralized BAS reaches a maximum value (at ~ 4 wt% Mo) for the series 15 and 25. Regardless of the Mo amount, the acidity stays constant for the two remaining series (SiAl = 40 and 75). Therefore, no molybdenum is anchored on the Brønsted acid sites for these two series. The limitation of the neutralized BAS with the Mo content points out the partial exchange of BAS.

This property was also identified by Xu et al. [42], who impregnated up to 15 wt% of molybdenum on HZSM-5 (SiAl = 25) and calculated the relative integrated intensity of pyridine adsorbed on Brønsted acid sites. They also found this band intensity decreases with the Mo loading until it reaches a maximum value at 6 wt%. With the help of H_2/D_2 exchange analysis, Iglesia et al. [34] showed a similar observation on HZSM-5 zeolite with a molar ratio SiAl = 14.3. Indeed the H_2O evolution rate is directly related to the Mo content for samples with 1.0–3.6 wt%. After reaching this value, the desorption rate becomes constant as the Mo content increases.

From Fig. 5b and Table 1, it is possible to assess the maximum reduction loss of BAS concentration after Mo impregnation, i.e, ~ 30, ~ 20, 0, 0% for SiAl = 15, 25, 40, and 75, respectively.

Rice et al. [43] calculated by stochastic simulations the probability in ZSM-5 zeolite of NNN pairs of Al atoms able to stabilize a divalent cation (M^{2+}) and form an oxo- binuclear cation, i.e., two M^{2+} bridged by an oxygen atom $(\text{-M-O-M-})^{2+}$. The assessment of the maximum probability to form bridged M^{2+} and oxo-binuclear cation depends on the molar Si/Al ratio and is summarized in Table S1.

The theoretically determined values for the proportion of stabilized oxo-binuclear cation are consistent with the BAS reduction concentration found for the molybdenum-supported catalysts. Therefore, the amount of Mo at the channel intersections is limited to the number of aluminum pairs. The remaining isolated protons are consequently not accessible during the molybdenum migration.

3.2. Activity and selectivity of the Mo/HZ-Y catalyst series

The catalytic performance of the X-MoHZ-Y samples in the dehydroaromatization of methane was then carried out. The samples showed the typical time-on-stream behavior of Mo/HZSM-5 with the three well-known steps [12,44]: (i) activation time where the benzene yield is null, (ii) then the aromatics yields increase in the first hour during the induction step (iii) followed by a slight decrease in the methane conversion and the benzene yield (Fig. 6). The induction and deactivation periods correspond to the production of aromatics. The area under the signal of Fig. 6 represents the cumulative yield of benzene throughout the whole reaction.

3.2.1. Carburization of the supported oxomolybdate zeolite X-HZ-Y: activation stage

From Fig. 6, it is possible to draw the activation time as a function of Mo contents for each different series (Fig. 7). It appears clearly that the activation time is directly related to the amount of molybdenum. This proportionality suggests a stoichiometry reaction between methane and molybdenum species.

Even if the carburized active species have still not been well established [45], the carburation occurs on both MoO_3 oxide phase segregated outside the channels [10,46,47] and the supported Mo_2O_5 dimers anchored within the zeolite channels by bridging two Al centers as visible in Eqs. 5 and 6, respectively.

$$4MoO_3 + 7CH_4 \rightarrow 2 \quad Mo_2C + 3CO_2 + 2CO + 10H_2 + 4H_2O \tag{5}$$

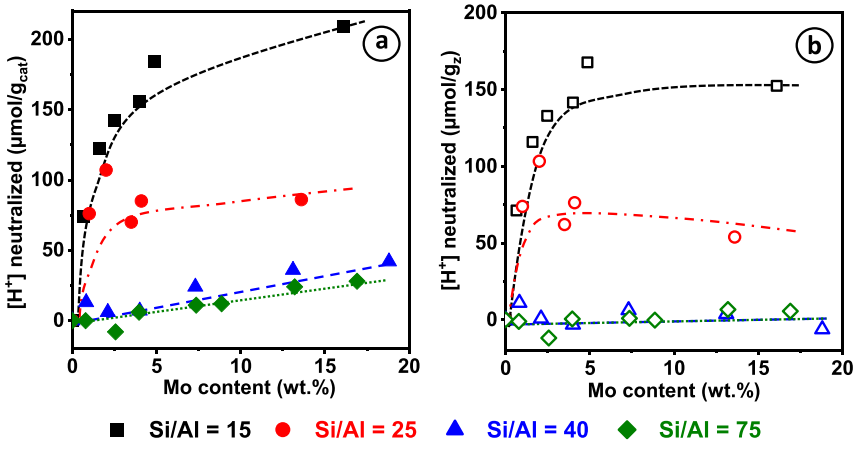

Fig. 5. : Amount of Brønsted acid sites neutralized after Mo impregnation as a function of the Mo loading for the different series of catalysts. The data in full and open symbols are normalized from the amount of catalyst (a) and zeolite (b), respectively.

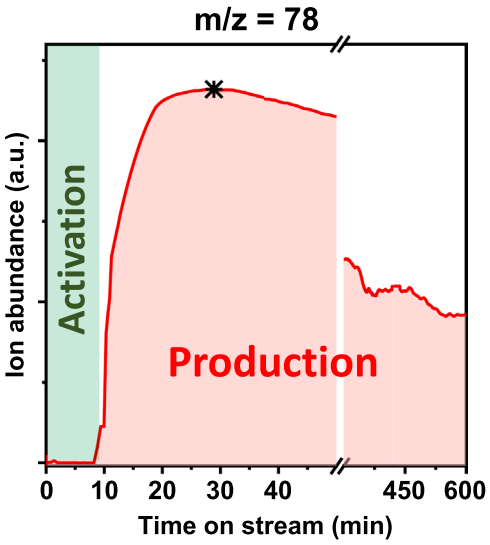

Fig. 6. : Mass spectra of the benzene as a function of time on stream. The red area corresponds to the cumulative yield of benzene and is possible to separate into two parts. Before (*)refers to the induction period and after (*) to the deactivation step.

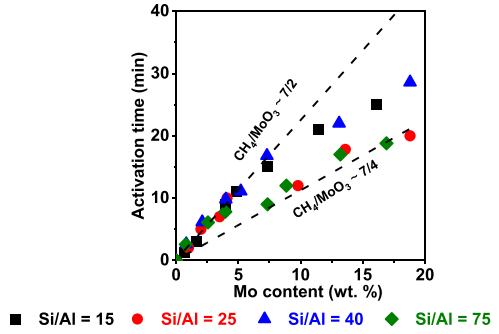

Fig. 7. Duration of the activation step as a function of the Mo loading for the different catalyst series.

$$2MoO_3 + 7CH_4 \rightarrow Mo_2C + 6CO + 14H_2 \quad (6)$$

The straight lines corresponding to the two different stoichiometry numbers were plotted. Most of the data were found in this range. Surprisingly, at high Mo loadings, this proportionally seems to decline. It results since full carburization of the molybdenum oxide is not necessary to start benzene production [30,48]. As numerous variety of molybdenum reduced centers such as MoC, α-Mo_2C_{1-x}, β-Mo_2C, MoO_xC_y, partially reduced MoO_{3-x} was reported [49] could therefore change the stoichiometry CH_4/oxides of the two previous equations.

3.2.1.1. Catalytic tests (Production stage). It can be seen in Fig. 8, the evolution of the cumulative product yields throughout the whole reaction as a function of the Mo loading for the different catalysts series.

First of all, it appears Mo is requisite to activate the catalyst. Indeed, all the protonic zeolites display negligible aromatics formation. The same conclusion emerges regarding the acidity of the zeolite. Since the Mo-supported silicate cumulative yields in Fig. S7 show no catalytic activity. Only the co-existence of metallic and acid functions leads to an active catalyst.

For all "acid" series, benzene is the main formed product followed by higher aromaticity compounds (mainly coke + naphthalene), then ethylene and toluene are found in small proportion. The results point out higher cumulative methane conversion for a lower Si/Al ratio, which agrees with previous works [22,23]. Furthermore, as explained by the

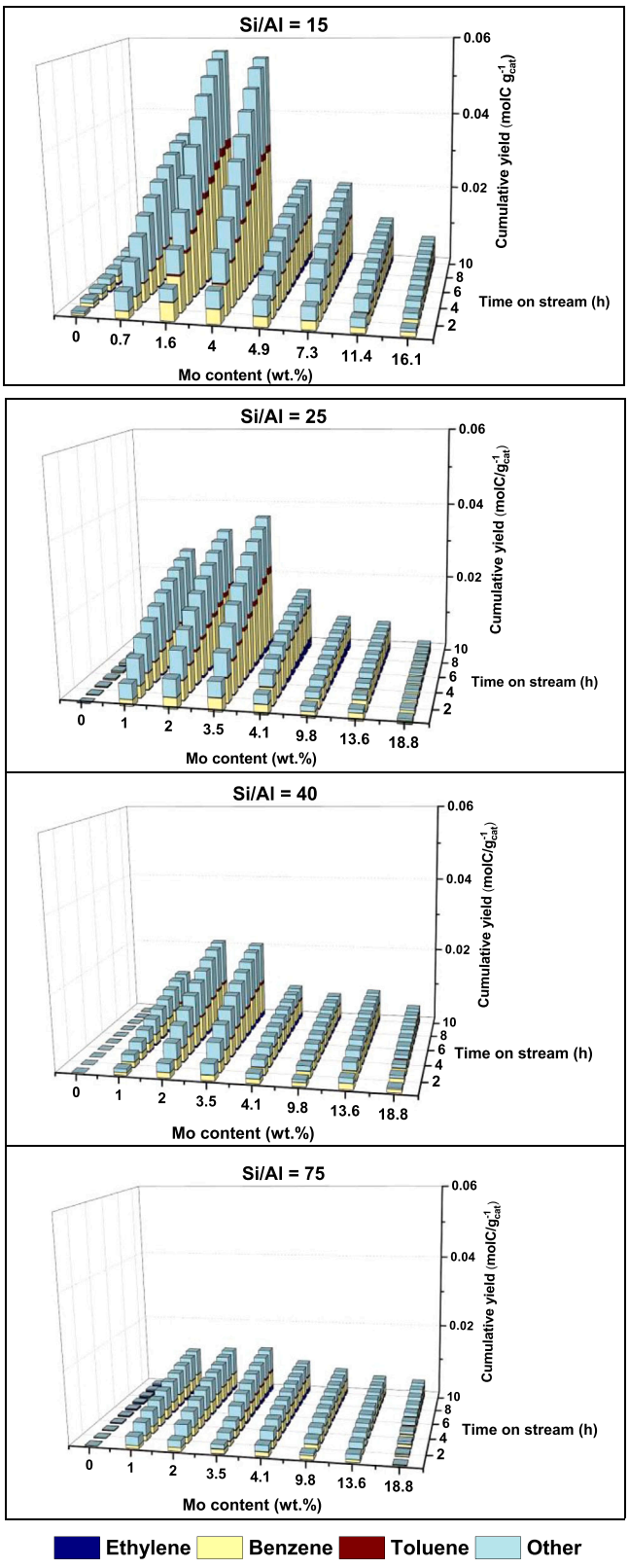

Fig. 8. Cumulative yield after 10 h of reaction of the different products as a function of the Mo loading for the different catalysts series.

chemisorption of pyridine at 150 °C, a lower Si/Al ratio promotes a higher probability of paired aluminum inside the zeolite channel where the Mo oxide precursors for the active sites strongly anchor.

Interestingly, regardless of the Brønsted acidity, the cumulative yields follow a bell-shaped curve. The accumulated products increase as a function of the Mo content until it reaches a maximum value, then it suddenly decreases. The ideal composition is obtained for 3–4 wt% Mo, which corresponds to previous reports [29,50]. Once the value is exceeded, a sudden drop of catalytic activity appears for all series.

Particular attention should be given at 1 h of reaction. Indeed, the induction period is assumed to be finished indicating the catalyst achieves its maximum activity. From Fig. S3**,** the induction period length is deduced, directly related to the Brønsted acidity. The higher is the BAS concentration, the longer this step is. More surprisingly, the induction time follows the same tendency as the cumulative yields, i.e., its length increases until the Mo loading reaches ~ 4 wt% and then a sudden drop once Mo content exceeds this value. The induction period becomes almost immediate in excess of Mo. Recently, it was proposed that this step corresponds to the building up of an organo-catalytic complex known as Hydrocarbon pool (HCP) [12,13,51]. This correlation between induction time and cumulative yields allows us to assume that these entities play a critical role in the MDA process by favoring the formation of the products.

Once the catalyst achieves its operational activity, it starts to deactivate. Since no drastic change in selectivity during the reaction is observed (Fig. 8), it supports the non-selective nature of deactivation [52]. An exponential function was assumed for catalyst deactivation, depending on the deactivation constant (k_d) and the time-on-stream [53] and exposed in Table 2 **(**Fig. S8**).** Besides the severe lack of methane conversion, high Mo loading catalysts present strong deactivation behavior regardless of the Si/Al ratio.

Consequently, an interesting relation emerges; three catalytic parameters are intrinsically linked: the cumulative benzene yield after 10 h, the deactivation constant (k_D), and the induction time. Fig. 9 shows the interconnection of these parameters. The more the catalyst produced benzene, the longer the induction time, and the slower the deactivation step. In summary, if the catalyst has a high activity, it will be more stable due to the autogenous produced hydrogen [54,55]. In addition, to achieve the operational activity, the accumulation of HCP should preferably be performed with a catalyst with a high acid site density.

3.3. Physico-chemical properties of the spent catalysts X-HZ-Y/Sp after 10 h of reaction

Further characterizations of the spent catalyst recovered after 10 h of reaction were performed and exhibited in Table 2**.**

First of all, the ICP measurements indicate no significant

Table 2
Characterizations of the spent catalysts recovered after 10 h of reaction.

Sample name	Mo (wt%)[a]	Deactivation rate[b] (h^{-1})	Carbidic coke[c] (wt%)	"Soft" coke[c] (wt%)	"Hard" coke[c] (wt%)	Micropore volume[d]	
						Value ($cm^3\ g_{cat}^{-1}$)	Reduction (%)
Series 15							
HZ-15/Sp		/	0	0.72	2.87	0.09	33
0.7-MoHZ-15/Sp		0.13	0	1.47	6.90	0.09	28
1.6-MoHZ-15/Sp	1.6	0.13	0	1.97	6.45	0.08	32
4.0-MoHZ-15/Sp		0.10	0.14	3.11	1.48	0.10	14
4.9-MoHZ-15/Sp	5.6	0.28	0.42	1.79	1.62	0.04	62
7.4-MoHZ-15/Sp		0.22	0.69	1.68	1.61	0.05	49
11.4-MoHZ-15/Sp		0.31	1.30	0.66	0.65	0.04	60
16.1-MoHZ-15/Sp	16.4	0.38	2.32	1.17	0.64	0.03	63
Series 25							
HZ-25/Sp		/	0	0	1.704	0.13	6
1.0-MoHZ-25/Sp		0.17	0	3.15	3.91	0.11	19
2.0-MoHZ-25/Sp	2.1	0.18	0	3.76	2.69	0.11	14
3.5-MoHZ-25/Sp		0.16	0	5.01	1.41	0.11	16
4.1-MoHZ-25/Sp	5.0	0.31	0.17	3.55	1.33	0.03	77
9.8-MoHZ-25/Sp		0.40	0.18	3.97	1.12	0.03	77
13.6-MoHZ-25/Sp	10.9	0.52	1.09	2.88	1.16	0.02	83
18.8-MoHZ-25/Sp		0.67	2.48	1.13	0.74	0.02	81
Series 40							
HZ-40/Sp		/	0	0	0	0.15	8
0.8-MoHZ-40/Sp	0.7	0.16	0	2.45	4.65	0.10	23
2.1-MoHZ-40/Sp		0.14	0.08	2.77	5.55	0.09	29
4.0-MoHZ-40/Sp	3.9	0.14	0.16	2.39	2.98	0.09	39
5.2-MoHZ-40/Sp	5.4	0.21	0.38	1.01	1.34	0.04	74
7.3-MoHZ-40/Sp		0.35	0.73	0.93	1.06	0.04	71
13.1-MoHZ-40/Sp		0.47	2.88	0.51	0.6	0.02	84
18.8-MoHZ-40/Sp	18.4	0.45	3.85	0.23	0.58	0.03	76
Serie 75							
HZ-75/Sp		/	0	0.41	0.76	0.14	92
0.8-MoHZ-/Sp 75	0.8	0.25	0	2.18	3.56	0.12	81
2.6-MoHZ-75/Sp		0.25	0	2.38	2.05	0.12	89
4.0-MoHZ-75/Sp		0.31	0.08	1.65	1.32	0.08	52
7.3-MoHZ-75/Sp		0.42	0.37	1.05	0.81	0.03	28
8.9-MoHZ-75/Sp		0.42	0.62	1.20	0.84	0.03	25
13.2-MoHZ-75/Sp	11.7	0.41	2.23	0.70	0.35	0.04	30
16.9-MoHZ-75/Sp	16.0	0.40	2.90	0.73	0.60	0.01	9
Silicalite							
Si		/	0	0	0.25	0.17	3
1.6-Si		/	0	0.39	0.37	0.15	6
2.6-Si		/	0.27	0.36	0.39	0.16	4
6.3-Si		/	0.86	/	/	0.14	8

[a]Mo content measured by ICP analysis, [b]the deactivation rate is the slope of the logarithmic plot [c]measured by thermogravimetry analysis and [d] The micropore volume (V_{micro}) was calculated from the t-plot curve using the Harkins-Jura method and a thickness range between 4.5 and 5.5 Å,

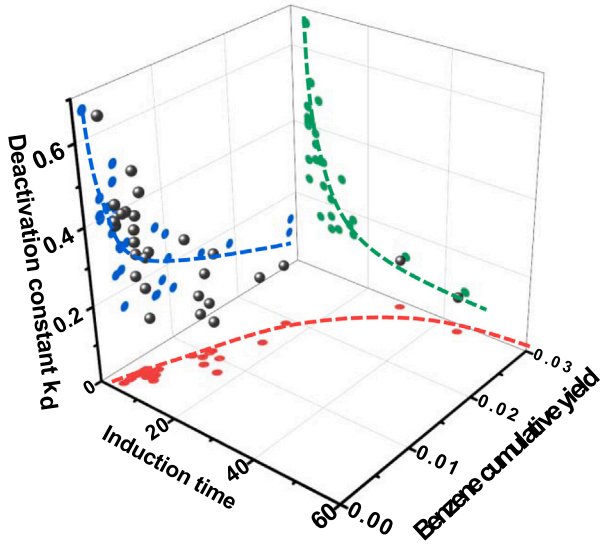

Fig. 9. Connection of the induction time, cumulative benzene yield after 10 h of reaction, and deactivation constant. Induction time as a function of the cumulative benzene yield (red) and the deactivation constant (blue), deactivation constant as a function of the cumulative benzene yield (green).

Molybdenum loss by potential sublimation (Table 2).

Thermogravimetric analysis followed by mass spectroscopy was carried out to investigate the combustion of coke species. All catalysts show similar weight loss profiles generally obtained for the MDA reaction (Fig. S4 and S5). From ~ 350 °C up to 500 °C, the initial weight gain is attributed to the carbide species (mostly Mo_2C) oxidation into MoO_3 [56]. A first weight loss up appears at 550 °C and a second at 650 °C. Both weight losses are more definite with the mass signal oxidation product, i.e., CO_2 ($m/z = 44$). Indeed, the combustion profiles can be deconvoluted into two well-defined peaks; the first and second peaks are ascribed to the oxidation of "soft" and "hard" coke, respectively [21]. Their quantities are drawn from the area of each peak.

Figure 10 compares the occupied microporous volume of the zeolite (Eq S3), the amount of "soft," "hard" coke, and the weight gain as a function of the molybdenum content for all catalysts series. For each series, it is possible to establish two distinct areas.

- $w_{Mo} < 4$ wt%, V^z_{micro}*occupied* slightly increases and stabilizes around 20%. Due to the low amount of molybdenum, no carbide oxidation occurs. Regardless of the acidity, the total coke amount increases until the Mo loading reaches 2 wt%. Then, it decreases as a function of the Mo loading. Regarding the coke nature, "hard" coke is predominant for the minimal Mo amount, i.e., $w_{Mo} < 2$ wt%. Once this value is exceeded, a curious change of coke distribution occurs. Coke is in the closest intimacy with Mo species, which can catalyze the coke combustion increasing; therefore, the "soft" coke contribution for Mo > 2 wt% [13]

- $w_{Mo} > 4$ wt%, V^z_{micro}*occupied* stay constant ca 80%. It appears clearly the higher the Mo loading, the higher the oxidation weight, which is directly related to the remaining amount of MoO_3 on the external zeolite surface of the fresh catalyst. For all series, the total coke is lower than 4 wt%. The contribution of "soft" coke is preponderant. It seems the total coke amount decreases when the Mo loading increases.

These earlier observations aroused our curiosity, as one would expect that the higher the amount of coke, the higher the occupied micropore volume. Commonly, the occupied volume should increase

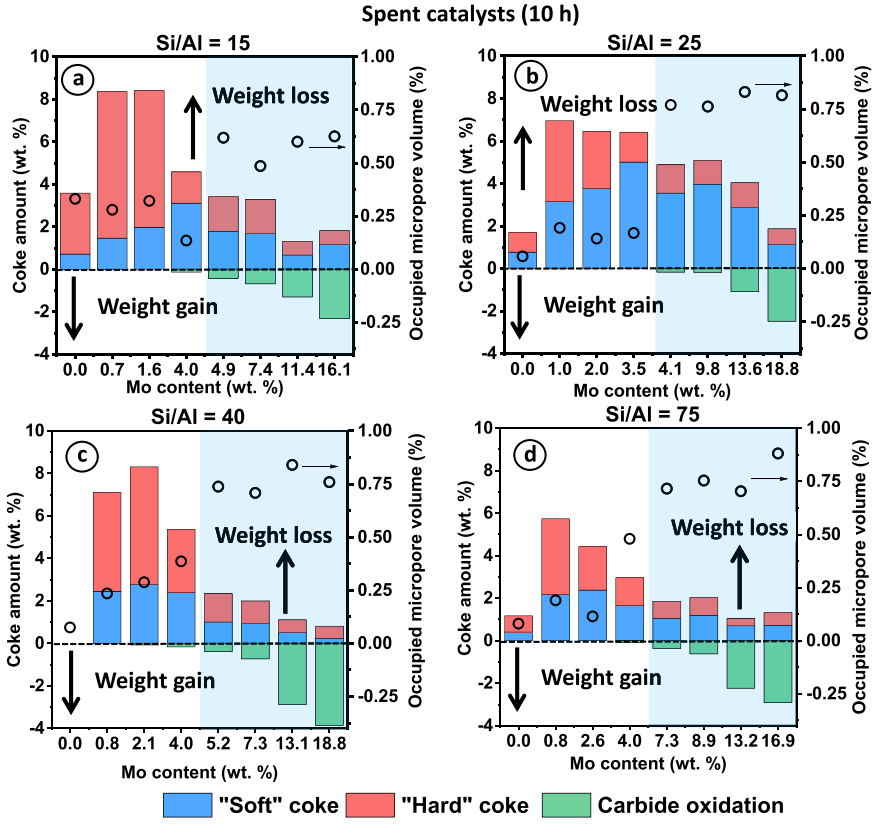

Fig. 10. : Coke content and occupied microporous volume of the spent catalysts recovered after 10 h of reaction as a function of the Mo loading for the different catalyst series: (a) SiAl = 15; (b) SiAl = 25; (c) SiAl = 40; and (d) SiAl = 75.

once the coke is deposited inside the zeolite channel on the isolated Brønsted acid site. Coke deposition could also recover the whole external zeolite surface blocking the access of the micropore. However, the insoluble coke molecules surround the zeolite crystallites when the total coke amount is higher than 7 wt% [57,58]. Thus, for high Mo loadings (Mo > 4 wt%), the micropore volume drop cannot be only attributed to partial pore blockage or coke accumulation on the external surface as it typically takes place during the MDA process [13,21].

Further XRD analyses performed on the spent samples (Fig. S9) confirm an important loss of peaks intensity when the Mo content increases regardless of the acidity. A large shoulder appears for $2\Theta = 22°$, indicating the presence of an amorphous phase. In addition, when the peaks intensity of the ZSM-5 decreases, new broad peaks start to increase at $2\theta = 39.5°$, characteristic of the species β-Mo_2C (JCPDS File No. 35–0787). This large shoulder suggests the overlap of the molybdenum carbide with some other amorphous carbon species [59].

The presence of a well-defined amorphous phase clearly evidences the start of a collapse of the internal zeolite structure once the Mo loading exceeds 4 wt%, which becomes more and more important as long as the Mo loading increases.

3.3.1. Discussion

The results indicate the requirement to control the balance between acid and metal function. Indeed, by studying the evolution of the physicochemical properties and the catalyst performance during the four successive stages: calcination, activation, and production (iii) stages, then deactivation period, two distinct domains appear as a function of the molybdenum content: W_{Mo} lower or higher than 4 wt%, This limit value corresponds to an optimal value whatever the Si/Al molar ratio.

3.3.2. Calcination stage

As the temperature increases during the calcination step, molybdenum oxide migrates inside the zeolite channel and reacts on BAS, which is more available on low Si/Al ratio [22,2460]. The partial BAS exchange observed with chemisorption of pyridine at 150 °C shows Mo solely anchored to bridged pair Al atoms. Thus, the maximum possible Mo to exchange is limited and depends on the zeolite acidity density.

The combination of Raman and IR studies confirms the statement made by lately published papers [34,61] in which the most stable adsorption structure for molybdenum within the ZSM-5 channels is dimer $Mo_2O_5^{2+}$ bridged at two Al atoms in 6MR-δ.

At low Si/Al (15, 25), the high acid site density allows the molybdenum to anchor on the Al paired. When the Mo loading is low (< 2 wt %), the monomeric bidentate species MoO_2^{2+} is firstly detected. Tessonier et al. reported this same anchoring behaviour where the formation of the monomer bridged to two Al appears only under very specific synthesis conditions, i.e., SiAl = 15 and Mo content < 2 wt% [19]. However, the monomers may not be likely to be stabilized, as shown by previous modeling calculations [51]. Then, when the Mo content start to increase, two similar monomers MoO_2^{2+} condense favorably into one anchored dimeric bidentate species $Mo_2O_5^{2+}$.

The characteristic peak of MoO_3 starts to appear when the Mo amount reaches 4. wt%. Once the Mo loading exceeds 4 wt%, a slight decrease of V_{micro} occurs for the series 15 due to $Al_2(MoO_4)_3$ formation. Its formation is mitigated since the calcination temperature is lower than 600 °C (i.e., 500 °C). The interactions between Mo moieties and the zeolite are not strong enough to dealuminate the zeolite framework, thus partially preserving the internal zeolite structure [9] (Scheme 1). XRD analyses and N_2-physisorption measurements confirm the high crystallinity of the material despite high Mo amounts.

3.3.3. Activation and production stages

To resume, the first parameter to consider for an optimal MDA reaction is the Brønsted acidity concentration. It allows dispersing the molybdenum active site precursor inside the zeolite channel during the calcination step. Then, once the molybdenum is reduced, its close proximity with the acidic proton enables the building-up of an organo-catalytic complex [62]. Fig. 8 and Scheme 2 show that if the protonic zeolite presents a high Si/Al molar ratio, the cumulative yield is constant regardless of Mo loading. For that reason, once the zeolite presents the suitable acidity, the second parameter to carefully factor is the molybdenum amount:

(i) W_{Mo} < 4 wt%. Impregnating a minimal amount of molybdenum initiates an active catalyst. However, the necessary Mo amount to build an ideal HCP is not achieved, limiting thus the cumulative yields.
(ii) W_{Mo} reaches the "ideal" value ~ 4 wt%. The optimal amount of molybdenum is impregnated on the catalyst allowing its high performance. The compromise between metal and acidity function leads to long induction and slow deactivation, which are requisite for maximum product formation.
(iii) W_{Mo} > 4 wt%: a sudden drop of catalytic activity regardless of the Brønsted acidity is noticed. In addition, the calculated deactivation constant k_d underlines a rapid loss of catalytic activity (Table 2) [53]. It highlights that only molybdenum drives the

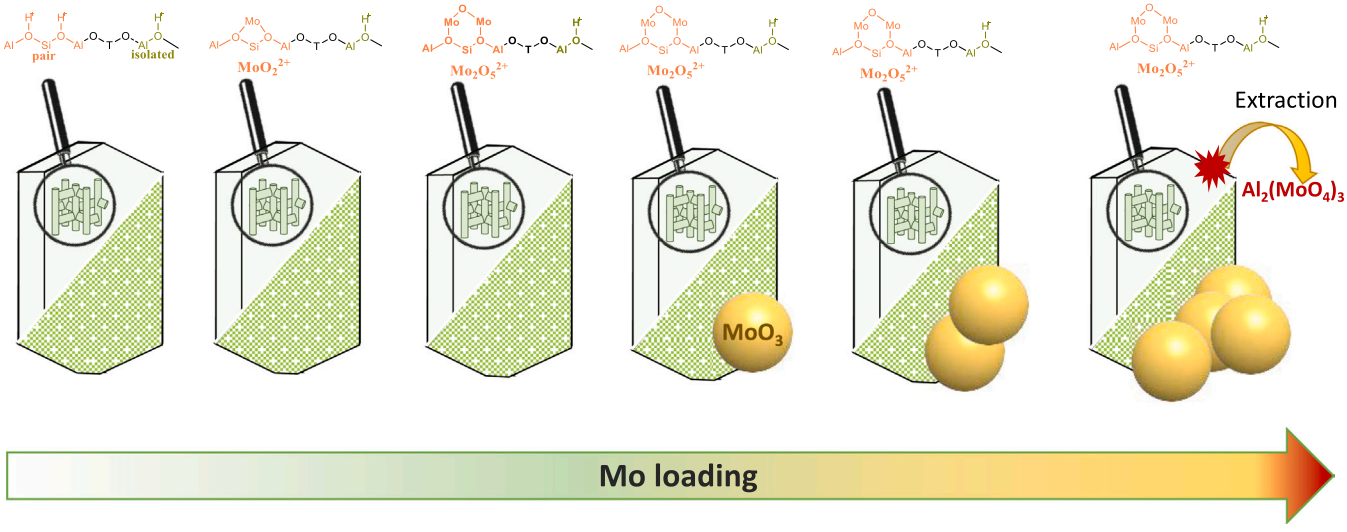

Scheme 1. Impact of the Mo loading on the textural properties of the zeolite after the calcination step.

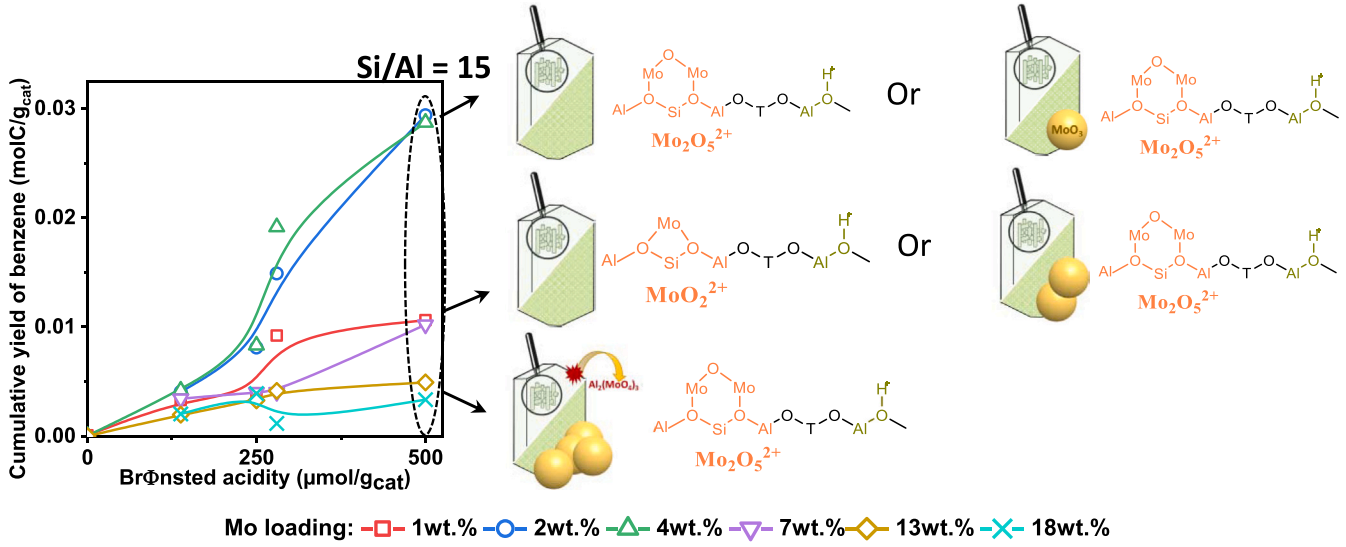

Scheme 2. Cumulative yield of benzene as a function of the initial Brønsted acidity for different Mo loading and establish of a structure-activity relationship for the series SiAl = 15.

reaction at this loading and is responsible for catalyst deactivation.

By assuming only $Mo_2O_5^{2+}$ moieties are anchored inside the zeolite channel, the amount of Mo involved in dimeric oxomolybdate supported on the zeolite framework is given by the following equation.

$$wMo_{Mo2O5} = [H^+]^{\Sigma}_{neutralized} * M_{Mo} * 100 \quad (4)$$

The maximum amounts of Mo anchored as dimer $Mo_2O_5^{2+}$ inside the zeolite channel are 1.4, 0.5, and 0 Mo wt% for the catalysts series SiAl = 15, 25, and 40 and 75, respectively. Once the Mo loading exceeds this maximum value, additional Mo remains at the external surface in the form of tridimensional MoO_3 crystallite (~ 90 nm), even if isolated reactive protons are still accessible. However, the four series exhibit the optimal activity for Mo loading ~ 4 wt%.

Two assumptions could explain this structure-activity behavior. First, the molybdenum migrates inside the zeolite channel during the pretreatment. It is worth mentioning that the calcination temperature is 500 °C, whereas the reaction occurs at 700 °C. Hensen et al. [63] investigated the effect of calcination temperature on the concentration of BAS and showed that low Mo content (< 3 wt%) initiates a slight reduction of BAS as the calcination temperature increases with no impact on the crystallinity. It suggests that Mo migrates inside the zeolite channels. Further Mo precursors for active sites are undetectable at 500 °C and are formed at higher temperatures. Thus, a textural properties change could occur under the inert pretreatment heating.

Another explanation is the external molybdenum species are active in the reaction. Indeed, a significant variety of molybdenum reduced centers such as MoC, α-Mo_2C_{1-x}, β-Mo_2C, partially reduced MoO_{3-x} on the outside surface were reported [49,64] to play possibly a role in this singular reaction. But to be active, these species require the presence of Brønsted acid sites (Fig. S6). This currently unresolved structure-activity relation emphasizes the complex nature of the involved reaction mechanism and the identification of the active sites (Scheme 2).

3.3.4. Deactivation step

The spent catalysts recovered after 10 h of reaction were deeply characterized to identify the deactivation modes.

- Mo < 4 wt%, N_2-physisorption measurements demonstrate that carbon species block the pores of 1% Mo and 4% Mo catalysts in a similar manner, independent of the Mo content. This is well-known as the polycondensation of the formed aromatics over the Brønsted acid sites on the external surface and at the cannel mouth leads to serious coke formation and catalyst deactivation. Thus the higher the acidity, the higher the total coke recovered on the catalyst.
- Mo > 4 wt%, a new deactivation mode has been identified in which the zeolite collapse after 10 h of reaction independent of the zeolite acidity. The strong deactivation constant and the brief induction period for high Mo loading suggest zeolite amorphization occurs in the early stage of the reaction. Fig. S6 represents products formation during the activation of the catalyst 16.9-MoHZ-75. It appears that H_2O and CO_2 are formed as long as the activation step lasts. As demonstrated previously, the higher the Mo content, the longer the activation is, thus producing a considerable amount of water that could potentially dealuminate the zeolite. For that reason, we presume the formation of water during the activation for carburizing the oxo-molybdate supported catalysts might contribute to the collapse of the zeolite. In addition, its low space velocity can also favor the dealumination of the zeolite. By considering only (Eq. 5) and a 20% constant molar conversion of methane, we reach a partial pressure of water equals p_{H2O} ~ 7%. Previous studies [64,65] show that co-feeding the methane flow with water is known to inhibit the reaction once the partial pressure p_{H2O} exceeds this critical value. Thus water plays a key role in the carburation of the molybdenum species. Hensen et al. [63] also suggested that H_2O formed during the regeneration step could contribute to the dealumination of the catalyst. They show similar behavior, in which the catalyst with more Mo loading was unstable upon reaction-regeneration cycle, independent of the Brønsted acidity. Thus, water seems to react preferentially with high Mo loading regardless of the Si/Al molar ratio. Limiting its production turns out to be indispensable. In addition, the pre-treatment under nitrogen at 700 °C also favors the apparition of extra-framework species, when the Mo content increases [63].

From the XRD pattern in Fig. S10, no significant loss of zeolite crystallinity and amorphous phase detection on the spent silicalite with high Mo loadings were noticed. In addition, the slight reduction of V_{micro} supports the high crystallinity of the spent aluminum-free samples. All these observations state the produced water and pre-treatment system impact only the "acid" series, thus confirming the dealumination process during the early stages of the reaction.

4. Conclusion

More than thirty catalysts with different Si/Al ratios and molybdenum loadings were prepared and tested in the methane non-oxidative dehydroaromatization to study the impact of the balance between metallic and acid functions. From these results, the best suitable compromise was then established where the catalyst is composed of 4 wt % Mo with the highest possible acidity. Then two distinctions emerge:

(i) $W_{Mo} < 4$ wt%: high acidity allows dispersing the Mo precursors of active sites inside the zeolite channel. From the identification, localization, and quantification, it suggests that Mo remaining on the external surface could also activate the catalyst. However, its amount is too low to reach optimal benzene productivity. Moreover, the presence of the Brønsted acid sites is a condition prerequisite to transforming methane into benzene.

(ii) $W_{Mo} > 4$ wt%: The activation step lasts longer with a larger amount of molybdenum. The high water production leads to molybdenum change of morphology and zeolite amorphization.

Therefore, the carburation conditions (temperature, space velocity, partial pressure, pre-treatment nature) are a key point to study in-depth and should not be ignored.

CRediT authorship contribution statement

Antoine Beuque: Conceptualization, Methodology, Validation, Investigation, Writing – original draft, Writing – review & editing. **Hao Hu:** Writing – review & editing. **Elise Berrier:** Resources, Writing – review & editing, Funding acquisition. **Alexander Sachse:** Writing – review & editing. **Jean-François Paul:** Resources, Writing – review & editing, Funding acquisition. **Ludovic Pinard:** Conceptualization, Methodology, Validation, Investigation, Resources, Writing – original draft, Writing – review & editing, Supervision, Funding acquisition

Declaration of Competing Interest

The authors declare the following financial interests/personal relationships which may be considered as potential competing interests: Ludovic Pinard reports financial support was provided by European Union.

Acknowledgments

The authors acknowledge financial support from the European Union (ERDF) and “Région Nouvelle Aquitaine”.

The authors thank the European Union’s Horizon 2020 research and innovation program for its funding under grant agreement No 814548. This publication only reflects the author’s views, wtand neither Agency nor the Commission is responsible for any use that may be made of the information contained therein.

Appendix A. Supporting information

Supplementary data associated with this article can be found in the online version at doi:10.1016/j.cattod.2022.06.001.

References

[1] 2021 BP, 1 72.
[2] 2021 Total Energies, 1 42.
[3] K. Huang, C.T. Maravelias, Synthesis and analysis of nonoxidative methane aromatization strategies, Energy Technol. (2019) 1–11, https://doi.org/10.1002/ente.201900650.
[4] P. Tang, Q. Zhu, Z. Wu, D. Ma, Methane activation: the past and future, Energy Environ. Sci. 7 (8) (2014) 2580–2591, https://doi.org/10.1039/C4EE00604F.
[5] N. Kosinov, E.J.M. Hensen, Reactivity, selectivity, and stability of zeolite-based catalysts for methane dehydroaromatization, Adv. Mater. 32 (44) (2020), 2002565, https://doi.org/10.1002/adma.202002565.
[6] P. Schwach, X. Pan, X. Bao, Direct conversion of methane to value-added chemicals over heterogeneous catalysts: challenges and prospects, Chem. Rev. 117 (13) (2017) 8497–8520, https://doi.org/10.1021/acs.chemrev.6b00715.
[7] S. Ma, X. Guo, L. Zhao, S. Scott, X. Bao, Recent progress in methane dehydroaromatization: from laboratory curiosities to promising technology, J. Energy Chem. 22 (1) (2013) 1–20, https://doi.org/10.1016/S2095-4956(13)60001-7.
[8] L. Wang, L. Tao, M. Xie, G. Xu, J. Huang, Y. Xu, Dehydrogenation and aromatization of methane under non-oxidizing conditions, Catal. Lett. 21 (1–2) (1993) 35–41, https://doi.org/10.1007/BF00767368.
[9] P.L. Tan, Y.L. Leung, S.Y. Lai, The effect of calcination temperature on the catalytic performance of 2 wt% Mo/HZSM-5 in methane aromatization, Appl. Catal. A: Gen. 228 (2002) 115–125, https://doi.org/10.1016/S0926-860X(01)00955-3.
[10] Y.-H. Kim, R.W. Borry, E. Iglesia, Genesis of methane activation sites in Mo-exchanged H–ZSM-5 catalysts, Microporous Mesoporous Mater. 35–36 (2000) 495–509, https://doi.org/10.1016/S1387-1811(99)00245-0.
[11] W. Ding, S. Li, D. Meitzner, G. Iglesia, E. Methane, Conversion to aromatics on Mo/H-ZSM5: structure of molybdenum species in working catalysts, J. Phys. Chem. B 105 (2) (2001) 506–513, https://doi.org/10.1021/jp0030692.
[12] N. Kosinov, E.J.M. Hensen, E.A. Uslamin, Confined carbon mediating dehydroaromatization of methane over Mo/ZSM-5, Angew. Chem. Int. Ed. 57 (4) (2018) 1016–1020.
[13] N. Kosinov, E.A. Uslamin, F.J.A.G. Coumans, A.S.G. Wijpkema, R.Y. Rohling, E.J. M. Hensen, Structure and evolution of confined carbon species during methane dehydroaromatization over Mo/ZSM-5, ACS Catal. 8 (9) (2018) 8459–8467, https://doi.org/10.1021/acscatal.8b02491.
[14] D. Ma, D. Wang, L. Su, Y. Shu, Y. Xu, X. Bao, Carbonaceous deposition on Mo/HMCM-22 catalysts for methane aromatization: a TP technique investigation, J. Catal. 208 (2) (2002) 260–269, https://doi.org/10.1006/jcat.2002.3540.
[15] H. Jiang, L. Wang, W. Cui, Y. Xu, Study on the induction period of methane aromatization over Mo/HZSM-5: partial reduction of mo species and formation of carbonaceous deposit, Catal. Lett. 57 (3) (1999) 95–102, https://doi.org/10.1023/A:1019087313679.
[16] Y. Xu, L. Lin, Recent advances in methane dehydro-aromatization over transition metal ion-modified zeolite catalysts under non-oxidative conditions, Appl. Catal. A: Gen. 188 (1) (1999) 53–67, https://doi.org/10.1016/S0926-860X(99)00210-0.
[17] E.J.M. Hensen, Methane dehydroaromatization by Mo/HZSM-5: mono- or bifunctional catalysis? ACS Catal. 7 (1) (2017) 520–529.
[18] S. Liu, L. Wang, R. Ohnishi, M. Ichikawa, Bifunctional catalysis of Mo/HZSM-5 in the Dehydroaromatization of Methane to Benzene and Naphthalene XAFS/TG/DTA/MASS/FTIR Characterization and Supporting Effects, J. Catal. 181 (2) (1999) 175–188, https://doi.org/10.1006/jcat.1998.2310.
[19] J.-P. Tessonnier, B. Louis, S. Walspurger, J. Sommer, M.-J. Ledoux, C. Pham-Huu, Quantitative measurement of the brönsted acid sites in solid acids: toward a single-site design of Mo-modified ZSM-5 Zeolite, J. Phys. Chem. B 110 (21) (2006) 10390–10395, https://doi.org/10.1021/jp0602629.
[20] Y. Song, Q. Zhang, Y. Xu, Y. Zhang, K. Matsuoka, Z.-G. Zhang, Coke accumulation and deactivation behavior of microzeolite-based Mo/HZSM-5 in the non-oxidative methane aromatization under cyclic CH4-H2 feed switch mode, Appl. Catal. A: Gen. 530 (2017) 12–20, https://doi.org/10.1016/j.apcata.2016.11.016.
[21] C. Tempelman, E.J.M. Hensen, On the deactivation of Mo/HZSM-5 in the methane dehydroaromatization reaction, Appl. Catal. B: Environ. 176–177 (2015) 731–739, https://doi.org/10.1016/j.apcatb.2015.04.052.
[22] K. Zhao, L. Jia, J. Wang, The influence of the Si/Al ratio of Mo/HZSM-5 on methane non-oxidative dehydroaromatization, New J. Chem. 43 (2019) 4130–4136.
[23] M. Rahman, A. Infantes-Molina, A.S. Hoffman, S.R. Bare, K.L. Emerson, S.J. Khatib, Effect of Si/Al ratio of ZSM-5 support on structure and activity of Mo species in methane dehydroaromatization, Fuel 278 (2020), 118290, https://doi.org/10.1016/j.fuel.2020.118290.
[24] A. Martínez, E. Peris, A. Vidal-Moya, Modulation of zeolite acidity by post-synthesis treatments in Mo/HZSM-5 catalysts for methane dehydroaromatization, Stud. Surf. Sci. Catal. 174 (2008) 1075–1080, https://doi.org/10.1016/S0167-2991(08)80072-9.
[25] A. Martínez, E. Peris, Non-oxidative methane dehydroaromatization on Mo/HZSM-5 catalysts: tuning the acidic and catalytic properties through partial exchange of zeolite protons with alkali and alkaline-earth cations, Appl. Catal. A: Gen. 515 (2016) 32–44, https://doi.org/10.1016/j.apcata.2016.01.044.
[26] C. Tempelman, E.J.M. Hensen, E.R.H. van Eck, Desilication and silylation of Mo/HZSM-5 for methane dehydroaromatization, Microporous Mesoporous Mater. 203 (2015) 259–273, https://doi.org/10.1016/j.micromeso.2014.10.020.
[27] U. Menon, M. Rahman, S.J. Khatib, A critical literature review of the advances in methane dehydroaromatization over multifunctional metal-promoted zeolite catalysts, Appl. Catal. A: Gen. 608 (2020), 117870, https://doi.org/10.1016/j.apcata.2020.117870.
[28] T. Pinglian, et al., Ammonia-basified 10 wt% Mo/HZSM-5 material with enhanced dispersion of Mo and performance for catalytic aromatization of methane, Appl. Catal. A: Gen. 580 (2019) 111–120.
[29] S.J. Khatib, M. Rahman, A. Sridhar, Impact of the presence of Mo carbide species prepared ex situ in Mo/HZSM-5 on the catalytic properties in methane aromatization, Appl. Catal. A: Gen. 558 (2018) 67–80.
[30] Increasing the catalytic stability by optimizing the formation of zeolite-supported Mo carbide species ex situ for methane dehydroaromatization - ScienceDirect ⟨htt

ps://www.sciencedirect.com/science/article/pii/S0021951719302465?dgcid=raven_sd_recommender_email⟩ (accessed 2020 -03 -13).
[31] J.L. Guth, H. Kessler, R. Wey, New route to pentasil-type zeolites using a non alkaline medium in the presence of fluoride ions, in: Y. Murakami, A. Iijima, J. W. Ward (Eds.), Studies in Surface Science and Catalysis, 28, New Developments in Zeolite Science and Technology; Elsevier, 1986, pp. 121–128, https://doi.org/10.1016/S0167-2991(09)60864-8.
[32] C. Miranda, J. Urresta, H. Cruchade, A. Tran, M. Benghalem, A. Astafan, P. Gaudin, T.J. Daou, A. Ramírez, Y. Pouilloux, A. Sachse, L. Pinard, Exploring the impact of zeolite porous voids in liquid phase reactions: the case of glycerol etherification by tert-butyl alcohol, J. Catal. 365 (2018) 249–260, https://doi.org/10.1016/j.jcat.2018.07.009.
[33] N. Maheswari, G. Muralidharan, Controlled synthesis of nanostructured molybdenum oxide electrodes for high performance supercapacitor devices, Appl. Surf. Sci. 416 (2017) 461–469, https://doi.org/10.1016/j.apsusc.2017.04.094.
[34] R.W. Borry, Y.H. Kim, A. Huffsmith, J.A. Reimer, E. Iglesia, Structure and density of Mo and acid sites in Mo-exchanged H-ZSM5 catalysts for nonoxidative methane conversion, J. Phys. Chem. B 103 (28) (1999) 5787–5796, https://doi.org/10.1021/jp990866v.
[35] J.-P. Tessonnier, B. Louis, S. Rigolet, M.J. Ledoux, C. Pham-Huu, Methane dehydro-aromatization on Mo/ZSM-5: about the hidden role of Brønsted acid sites, Appl. Catal. A: Gen. 336 (1) (2008) 79–88, https://doi.org/10.1016/j.apcata.2007.08.026.
[36] Ignacio, J.; et al. Polyoxometalates as Alternative Mo Precursors for Methane Dehydroaromatization on Mo/ZSM-5 and Mo/MCM-22 Catalysts. *Catalysis Science and Technology* 2019, No. 21.
[37] M.A. Banares, H.C. Hu, I.E. Wachs, Genesis and stability of silicomolybdic acid on silica-supported molybdenum oxide catalysts: in-situ structural-selectivity study on selective oxidation reactions, J. Catal. 155 (2) (1995) 249–255, https://doi.org/10.1006/jcat.1995.1207.
[38] H. Hu, I.E. Wachs, S.R. Bare, Surface structures of supported molybdenum oxide catalysts: characterization by Raman and Mo L3-edge XANES, J. Phys. Chem. 99 (27) (1995) 10897–10910, https://doi.org/10.1021/j100027a034.
[39] E. Haro-Poniatowski, M. Jouanne, J.F. Morhange, C. Julien, R. Diamant, M. Fernández-Guasti, G.A. Fuentes, J.C. Alonso, Micro-Raman characterization of WO3 and MoO3 thin films obtained by pulsed laser irradiation, Appl. Surf. Sci. 127–129 (1998) 674–678, https://doi.org/10.1016/S0169-4332(97)00724-1.
[40] Konnov, S.V.; Dubray, F.; Clatworthy, E.B.; Kouvatas, C.; Gilson, J.-P.; Dath, J.-P.; Minoux, D.; Aquino, C.; Valtchev, V.; Moldovan, S.; Koneti, S.; Nesterenko, N.; Mintova, S. Novel Strategy for the Synthesis of Ultra-Stable Single-Site Mo-ZSM-5 Zeolite Nanocrystals. *Angewandte Chemie International Edition n/a* (n/a). https://doi.org/10.1002/anie.202006524.
[41] F. Dubray, S. Moldovan, C. Kouvatas, J. Grand, C. Aquino, N. Barrier, J.-P. Gilson, N. Nesterenko, D. Minoux, S. Mintova, Direct evidence for single molybdenum atoms incorporated in the framework of MFI zeolite nanocrystals, J. Am. Chem. Soc. 141 (22) (2019) 8689–8693, https://doi.org/10.1021/jacs.9b02589.
[42] W. Liu, Y. Xu, Methane dehydrogenation and aromatization over Mo/HZSM-5: in situ FT–IR characterization of its acidity and the interaction between Mo species and HZSM-5, J. Catal. 185 (2) (1999) 386–392, https://doi.org/10.1006/jcat.1999.2515.
[43] M.J. Rice, A.K. Chakraborty, A.T. Bell, Al Next nearest neighbor, ring occupation, and proximity statistics in ZSM-5, J. Catal. 186 (1) (1999) 222–227, https://doi.org/10.1006/jcat.1999.2544.
[44] I. Vollmer, N. Kosinov, Á. Szécsényi, G. Li, I. Yarulina, E. Abou-Hamad, A. Gurinov, S. Ould-Chikh, A. Aguilar-Tapia, J.-L. Hazemann, E. Pidko, E. Hensen, F. Kapteijn, J. Gascon, A site-sensitive quasi-in situ strategy to characterize Mo/HZSM-5 during activation, J. Catal. 370 (2019) 321–331, https://doi.org/10.1016/j.jcat.2019.01.013.
[45] R. Ismagilov Z, V. Matus E, T. Tsikoza L, Direct conversion of methane on Mo /ZSM-5 catalysts to produce benzene and hydrogen: achievements and perspectives, Energy Environ. Sci. 1 (5) (2008) 526–541, https://doi.org/10.1039/B810981H.
[46] D. Ma, Y. Shu, M. Cheng, Y. Xu, X. Bao, On the induction period of methane aromatization over Mo-based catalysts, J. Catal. 194 (1) (2000) 105–114, https://doi.org/10.1006/jcat.2000.2908.
[47] D. Ma, Y. Shu, W. Zhang, X. Han, Y. Xu, X. Bao, In Situ 1H MAS NMR spectroscopic observation of proton species on a Mo-modified HZSM-5 zeolite catalyst for the dehydroaromatization of methane, Angew. Chem. Int. Ed. 39 (16) (2000) 2928–2931, https://doi.org/10.1002/1521-3773(20000818)39:16<2928::AID-ANIE2928>3.0.CO;2-T.
[48] D. Ma, Y. Shu, X. Bao, Y. Xu, Methane dehydro-aromatization under nonoxidative conditions over Mo/HZSM-5 catalysts: EPR study of the Mo species on/in the HZSM-5 zeolite, J. Catal. 189 (2) (2000) 314–325, https://doi.org/10.1006/jcat.1999.2704.
[49] I. Vollmer, I. Yarulina, F. Kapteijn, J. Gascon, Progress in developing a structure-activity relationship for the direct aromatization of methane, ChemCatChem 11 (1) (2019) 39–52, https://doi.org/10.1002/cctc.201800880.
[50] P. Tan, The catalytic performance of Mo-impregnated HZSM-5 zeolite in CH4 aromatization: strong influence of Mo loading and pretreatment conditions, Catal. Commun. 103 (2018) 101–104.
[51] A. Beuque, H. Hao, E. Berrier, N. Batalha, A. Sachse, J.-F. Paul, L. Pinard, How do the products in methane dehydroaromatization impact the distinct stages of the reaction? Appl. Catal. B: Environ. 309 (2022), 121274 https://doi.org/10.1016/j.apcatb.2022.121274.
[52] N.K. Razdan, A. Bhan, Carbidic Mo is the sole kinetically-relevant active site for catalytic methane dehydroaromatization on Mo/H-ZSM-5, J. Catal. 389 (2020) 667–676, https://doi.org/10.1016/j.jcat.2020.06.035.
[53] O. Levenspiel, Experimental search for a simple rate equation to describe deactivating porous catalyst particles, J. Catal. 25 (2) (1972) 265–272, https://doi.org/10.1016/0021-9517(72)90227-8.
[54] Y. Song, Y. Xu, Y. Suzuki, H. Nakagome, X. Ma, Z.-G. Zhang, The distribution of coke formed over a multilayer Mo/HZSM-5 fixed bed in H2 Co-fed methane aromatization at 1073K: exploration of the coking pathway, J. Catal. 330 (2015) 261–272, https://doi.org/10.1016/j.jcat.2015.07.017.
[55] H. Ma, R. Kojima, S. Kikuchi, M. Ichikawa, Effective coke removal in methane to benzene (MTB) reactionon Mo/HZSM-5 catalyst by H2 and H2O co-addition to methane, Catal. Lett. 104 (1) (2005) 63–66, https://doi.org/10.1007/s10562-005-7437-y.
[56] H. Liu, T. Li, B. Tian, Y. Xu, Study of the carbonaceous deposits formed on a Mo/HZSM-5 Catalyst in methane dehydro-aromatization by using TG and temperature-programmed techniques, Appl. Catal. A: Gen. 213 (1) (2001) 103–112, https://doi.org/10.1016/S0926-860X(00)00883-8.
[57] M. Guisnet, P. Magnoux, Coking and deactivation of zeolites: influence of the pore structure, Appl. Catal. 54 (1) (1989) 1–27, https://doi.org/10.1016/S0166-9834(00)82350-7.
[58] M. Guisnet, L. Costa, F.R. Ribeiro, Prevention of zeolite deactivation by coking, J. Mol. Catal. A: Chem. 305 (1) (2009) 69–83, https://doi.org/10.1016/j.molcata.2008.11.012.
[59] P. Liang, H. Gao, Z. Yao, R. Jia, Y. Shi, Y. Sun, Q. Fan, H. Wang, Simple synthesis of ultrasmall β-Mo2C and α-MoC1−x nanoparticles and new insights into their catalytic mechanisms for dry reforming of methane, Catal. Sci. Technol. 7 (15) (2017) 3312–3324, https://doi.org/10.1039/C7CY00708F.
[60] I. Vollmer, et al., Quantifying the impact of dispersion, acidity and porosity of Mo/HZSM-5 on the performance in methane dehydroaromatization, Appl. Catal. A: Gen. 574 (2019) 144–150.
[61] H. Liu, W. Shen, X. Bao, Y. Xu, Methane dehydroaromatization over Mo/HZSM-5 catalysts: the reactivity of MoCx species formed from MoOx associated and non-associated with brönsted acid sites, Appl. Catal. A: Gen. 295 (1) (2005) 79–88, https://doi.org/10.1016/j.apcata.2005.08.011.
[62] Gao, W.; Qi, G.; Wang, Q.; Wang, W.; Li, S.; Hung, I.; Gan, Z.; Xu, J.; Deng, F. Dual Active Sites on Molybdenum/ZSM-5 Catalyst for Methane Dehydroaromatization: Insights from Solid-State NMR Spectroscopy. *Angewandte Chemie International Edition n/a* (n/a). https://doi.org/10.1002/anie.202017074.
[63] N. Kosinov, F.J. a G. Coumans, G. Li, E.A. Uslamin, B. Mezari, A.S.G. Wijpkema, E. A. Pidko, E.J.M. Hensen, Stable Mo/HZSM-5 methane dehydroaromatization catalysts optimized for high-temperature calcination-regeneration, J. Catal. (2017) 346, https://doi.org/10.1016/j.jcat.2016.12.006.
[64] M. Çağlayan, A.L. Paioni, B. Dereli, G. Shterk, I. Hita, E. Abou-Hamad, A. Pustovarenko, A.-H. Emwas, A. Dikhtiarenko, P. Castaño, L. Cavallo, M. Baldus, A.D. Chowdhury, J. Gascon, Illuminating the intrinsic effect of water co-feeding on methane dehydroaromatization: a comprehensive study, ACS Catal. (2021) 11671–11684, https://doi.org/10.1021/acscatal.1c02763.
[65] H.S. Lacheen, E. Iglesia, Isothermal activation of Mo2O52+–ZSM-5 precursors during methane reactions: effects of reaction products on structural evolution and catalytic properties, Phys. Chem. Chem. Phys. 7 (3) (2005) 538–547, https://doi.org/10.1039/B415166F.